Title

Shadowgraph Measurements of Rotating Convective Planetary Core-Style Flows

Journal

Journal of Geophysical Research Planets, 129(9)

ISSN

2169-9097

Authors

Abbate, Jewel A

Aurnou, Jonathan M

Publication Date

2024-09-01

DOI

10.1029/2024je008471

JGR Planets

RESEARCH ARTICLE
10.1029/2024JE008471

Shadowgraph Measurements of Rotating Convective Planetary Core-Style Flows

Jewel A. Abbate[1] and **Jonathan M. Aurnou**[1]

[1]Department of Earth, Planetary, and Space Sciences, University of California, Los Angeles, Los Angeles, CA, USA

Key Points:

- Laboratory convection experiments simulate turbulent flows within the polar regions of planetary cores and subsurface oceans
- The convective flow scale, measured via shadowgraph imaging, agrees with both the critical and turbulent scale predictions
- This agreement cannot be explained without advancement in convection theory, and implies mean field dynamo action occurs in Earth's core

Correspondence to:
J. A. Abbate,
jewelabbate@ucla.edu

Citation:
Abbate, J. A., & Aurnou, J. M. (2024). Shadowgraph measurements of rotating convective planetary core-style flows. *Journal of Geophysical Research: Planets*, *129*, e2024JE008471. https://doi.org/10.1029/2024JE008471

Received 2 MAY 2024
Accepted 4 AUG 2024

Author Contributions:

Conceptualization: Jewel A. Abbate, Jonathan M. Aurnou
Data curation: Jewel A. Abbate
Formal analysis: Jewel A. Abbate, Jonathan M. Aurnou
Funding acquisition: Jewel A. Abbate, Jonathan M. Aurnou
Investigation: Jewel A. Abbate
Methodology: Jewel A. Abbate, Jonathan M. Aurnou
Project administration: Jewel A. Abbate, Jonathan M. Aurnou
Resources: Jonathan M. Aurnou
Supervision: Jonathan M. Aurnou
Validation: Jewel A. Abbate, Jonathan M. Aurnou
Visualization: Jewel A. Abbate
Writing – original draft: Jewel A. Abbate
Writing – review & editing: Jewel A. Abbate, Jonathan M. Aurnou

Abstract The local scale of rotating convection, ℓ, is a fundamental parameter in many turbulent geophysical and astrophysical fluid systems, yet it is often poorly constrained. Here we conduct rotating convection laboratory experiments analogous to convecting flows in planetary cores and subsurface oceans to obtain measurements of the local scales of motion. Utilizing silicone oil as the working fluid, we employ shadowgraph imagery to visualize the flow, from which we extract values of the characteristic cross-axial scale of convective columns and plumes. These measurements are compared to the theoretical values of the critical onset length scale, ℓ_{crit}, and the turbulent length scale, ℓ_{turb}. Our experimentally obtained length scale measurements simultaneously agree with both the onset and turbulent scale predictions across three orders of magnitude in convective supercriticality $\left(10^2 \lesssim \widetilde{Ra} \lesssim 10^5\right)$, a correlation that is consistent with inferences made in prior studies. We further explore the nature of this correlation and its implications for geophysical and astrophysical systems.

Plain Language Summary Turbulent convection occurs within the liquid metal, water, and gaseous fluid layers of planetary interiors such as Earth's molten iron outer core, the subsurface oceans of icy moons, and the deep atmospheres of gas planets, respectively. The flow in each of these systems is strongly affected by the rotation of the planetary body. This rotation organizes the convecting flow into columnar structures elongated in the direction of the rotation axis. The horizontal width of the columnar flows is known as the local length scale of rotating convection, and is crucially the scale at which important planetary phenomena are driven, such as the induction of Earth's magnetic field. However, this quantity is not well known for geophysical systems. Here we conduct rotating convection laboratory experiments analogous to the convecting flows in planetary interiors, in which the local length scale is measured using a visualization technique called shadowgraph imaging. We compare our measurements to theoretical scaling arguments for laminar and turbulent rotating flows, and find a simultaneous agreement with both. This heretofore unappreciated correlation with both theoretical scales presents difficulties when interpreting laboratory and numerical experimental results in the context of more extreme geophysical flows, a challenge we address in the discussion.

1. Introduction

Buoyancy-driven convection plays a vital role in shaping many geophysical and astrophysical flow phenomena, such as magnetic field-generating dynamo action in planetary and stellar interiors and the transport of materials within subsurface oceans of icy moons (e.g., Soderlund, 2019; Yadav, Gastine, Christensen, Wolk, & Poppenhaeger, 2016). In these systems, convection, fueled by density imbalances of compositional or thermal origin, takes the form of rotating columnar flows elongated in the direction of the planetary rotation axis (e.g., Aurnou et al., 2015; Sprague et al., 2006). For laminar flows, the axially aligned columnar flows can extend all the way across the fluid layer, and may attain the "global" axial length scale H. This quantity is well known for Earth's core via seismological measurements (e.g., Dziewonski & Anderson, 1981; Kennett, 2020), and can be broadly estimated for subsurface oceans of icy satellites from spacecraft data (see Nimmo & Pappalardo, 2016). The horizontal cross-axial width of the convective flow structures is defined by the local flow dynamics, and is called the "local" convective scale, ℓ. It is likely that convective energy is injected into planetary fluid layers at this scale (Calkins, 2018; Calkins et al., 2021; Schwaiger et al., 2019). Further, these local scale convective flows likely drive the formation of large-scale phenomena such as jets and vortices (Böning et al., 2023; Lonner et al., 2022; Stellmach et al., 2014), and generate local-scale induction that can cascade upscale to form planetary and stellar-scale magnetic fields (Aubert et al., 2017; Roberts & King, 2013; Tobias, 2021; Yan & Calkins, 2022).

Geophysical values of ℓ, however, are not well-constrained. This quantity cannot be directly observed for planetary interior fluid layers, nor sensed indirectly with typical remote sensing techniques. Rather, fluid

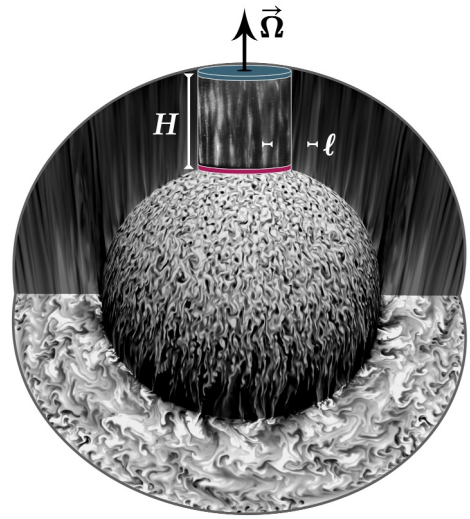

Figure 1. Schematic demonstrating the scales of a cylindrical laboratory experiment relative to a spherical shell numerical simulation of a planetary core. The cylinder outline at the pole of the sphere represents the aspect ratio $\Gamma \simeq 1$ convection cell used in this study, where the black arrow indicates the rotation vector $\vec{\Omega}$. A laboratory flow visualization conducted using water seeded with Kalliroscope particles is inset within the cylinder to demonstrate the flow patterns produced by cylindrical rotating convection relative to those of a spherical shell simulation of comparable dimensionless parameters. The global length scale, H, is drawn as a vertical white scale bar spanning the height of the convection cell and the spherical shell thickness. The local length scale, ℓ, is drawn as a horizontal scale bar for each the laboratory and numerical case indicating the width of a convective flow structure. The laboratory case is from Abbate and Aurnou (2023) with $Pr \simeq 6$, $Ra \simeq 2 \times 10^9$, $E \simeq 3 \times 10^{-6}$, $Ro_c \simeq 0.05$. The numerical simulation is from Gastine et al. (2016) with $Pr = 1$, $Ra \simeq 3 \times 10^9$, $E = 1 \times 10^{-6}$, $Ro_c \simeq 0.05$.

dynamical models built from theory and laboratory-numerical results are used to probe what physical balances persist, and to ascertain how those balances yield local scale dynamics capable of generating the large-scale flows observed at the surface (e.g., Aubert et al., 2017; Aurnou & King, 2017; Calkins et al., 2015; Christensen, 2010; Davidson, 2013; Guervilly et al., 2019). Laboratory experiments are often used to measure flow characteristics like heat transfer and flow velocity across a wide parameter range to generate scaling laws that can be extrapolated to planetary settings (e.g., Abbate & Aurnou, 2023; Aubert et al., 2001; Cheng et al., 2015, 2020; Gillet et al., 2007; Hawkins et al., 2023; King et al., 2012; Liu & Ecke, 1997; Lu et al., 2021; Rossby, 1969; Vogt et al., 2021; Wedi et al., 2021). Spatial velocity scales are far less often measured due to challenges in rotating flow imaging. However, constraints on ℓ are essential to produce accurate models of core dynamics.

Here we examine flow length scales within rotating convection laboratory experiments, which serve as analogs to convecting flows in planetary interior fluid layers. A schematic demonstrating our laboratory geometry relative to the typical spherical shell geometry considered for planets is presented in Figure 1. Shown is a snapshot of a rotating, convecting, hydrodynamic spherical shell simulation from Gastine et al. (2016). Inset at the pole, aligned with the rotation axis, is an image from a laboratory experiment conducted at similar dimensionless parameters in a water-filled cylindrical tank from Abbate and Aurnou (2023). The pink bottom boundary indicates the source of heating for the experiment, the blue top indicates cooling, and the black arrow represents the rotation vector $\vec{\Omega}$. The global and local length scales are marked in white as H and ℓ, respectively. When the global scale of the laboratory image (cylinder height) is scaled to match that of the simulation (shell thickness), the cross-axial scale of the convective flows, as well as the overall flow patterns, compare remarkably well to one another. The convection experiments conducted here can thus serve as analogs for the flows that persist in the polar regions of systems with spherical shell geometry, such as planetary cores or subsurface oceans (cf. Gastine & Aurnou, 2023).

We focus our study on the cross-axial convective length scale ℓ, which is challenging to extract in laboratory settings. Early experiments employed visualization methods such as long-exposure particle tracing and thermotropic liquid-crystals (e.g., Nakagawa & Frenzen, 1955; Sakai, 1997). More recently, particle image velocimetry (PIV) has been implemented to quantitatively characterize the horizontal flow field (Kunnen et al., 2010; Madonia et al., 2021; Shi et al., 2020). However, these measurements are difficult to make in a closed, no-slip, rapidly rotating convection cell. Here, we choose to adopt a qualitative visualization-based approach. Utilizing

Table 1
Non-Dimensional Parameter Definitions for the Rotating Rayleigh-Bénard Convection (RRBC) System

Parameter	Definition	Meaning
Rayleigh	$Ra = \alpha g \Delta T H^3/(\nu\kappa)$	(thermal buoyancy)/(visc. and therm. diffusion)
Ekman	$E = \nu/(2\Omega H^2)$	(viscous diffusion)/(Coriolis)
Prandtl	$Pr = \nu/\kappa$	(viscous diffusion)/(thermal diffusion)
Nusselt	$Nu = qH/(k\Delta T)$	(total heat flux)/(conductive heat flux)
Global Reynolds	$Re_H = uH/\nu$	(inertial advection)/(viscous diffusion)
Global Rossby	$Ro_H = u/(2\Omega H) = Re_H E$	(inertial advection)/(Coriolis)
Convective Rossby	$Ro_c = \left(RaE^2/Pr\right)^{1/2}$	(thermal buoyancy)/(Coriolis)
Local Reynolds	$Re_\ell = u\ell/\nu = Re_H(\ell/H)$	(local-scale advection)/(viscous diffusion)
Local Rossby	$Ro_\ell = u/(2\Omega\ell) = Ro_H(H/\ell)$	(local-scale advection)/(Coriolis)

Note. The variables and units used in the definitions are the following: ν (viscosity, m^2/s), κ (thermal diffusivity, m^2/s), α (thermal expansivity, 1/K), g (gravitational acceleration, m/s^2), ΔT (vertical temperature drop, K), H (layer height, m), Ω (rotation rate, rad/s), q (total heat flux, W/m^2), k (thermal conductivity, W/m/K), u (flow velocity, m/s), ℓ (local scale of convection, m).

shadowgraph imagery, we extract measurements of the cross-axial scale of convective columns and plumes to compare with theoretical predictions. Silicone oil is used as the working fluid, because its strongly temperature-dependent refractive properties enable the visualization of shadow patterns as relatively warm and cool plumes move through the background fluid. Further, silicone oil is defined by moderate to large thermal Prandtl numbers ($Pr \approx 10^1$–10^3; defined in Section 2), which makes it a good proxy for compositional convection in Earth's outer core ($Pr \approx 10^2$–10^3) and for thermal convection in magma oceans ($Pr \approx 10^1$–10^2) (Abbate & Aurnou, 2023; Bouffard et al., 2019; Calkins et al., 2012).

2. Rotating Rayleigh-Bénard Convection (RRBC)

The canonical model employed to study these flows is that of rotating Rayleigh-Bénard convection (RRBC), in which a fluid layer is heated from below, cooled from above, and rotated about a vertical axis. The RRBC system has been studied extensively in the laboratory (Cheng et al., 2015, 2020; Hawkins et al., 2023; King et al., 2012; Kunnen et al., 2010; Lu et al., 2021; Madonia et al., 2023; Weiss & Ahlers, 2011). Its dimensionless control parameters are the Rayleigh number, $Ra = \alpha g \Delta T H^3/(\nu\kappa)$, defined as the strength of thermal buoyancy over diffusion; the Ekman number, $E = \nu/(2\Omega H^2)$, defined as the strength of viscous diffusion over the Coriolis force; and the Prandtl number, $Pr = \nu/\kappa$, defined as the ratio of viscous to thermal diffusion. Here, α is the thermal expansivity, ν is the kinematic viscosity, κ is the thermal diffusivity, g is gravitational acceleration, H is the fluid layer height, ΔT is the temperature difference across the fluid layer, and Ω is the angular rotation rate. Summarized definitions of the system parameters are provided in Table 1.

RRBC is further characterized by the convective Rossby number, $Ro_c = \left(RaE^2/Pr\right)^{1/2}$, which estimates the strength of rotational effects acting on the scale of the convection ℓ (Aurnou et al., 2020). Convective flows with $Ro_c \ll 1$ are strongly influenced by rotation, whereas those with $Ro_c \gg 1$ are largely uninfluenced by rotation (e.g., Camisassa & Featherstone, 2022; Gastine et al., 2013). The effect of rotation is additionally characterized by the supercriticality of the convective flow, $\widetilde{Ra} = Ra/Ra_c$, where Ra_c is the critical Rayleigh number, which defines the minimum Rayleigh number (buoyancy forcing) required for convection to occur given a fixed Ekman number (rotation period). In low E, $Pr > 0.68$ planar systems with no-slip top and bottom boundaries, convective supercriticality varies as $Ra_c = (8.7 - 9.63E^{1/6})\,E^{-4/3}$ (Kunnen, 2021; Niiler & Bisshopp, 1965). Therefore, a system is subcritical to convection if $\widetilde{Ra} < 1$, and it is convectively supercritical if $\widetilde{Ra} > 1$.

Theoretical RRBC predictions can be determined from a local torque balance between relevant terms in the vorticity equation (Abbate & Aurnou, 2023; Aubert et al., 2001; Cardin & Olson, 1994; Ingersoll & Pollard, 1982; Madonia et al., 2023; Nicoski et al., 2024). Here, predictions are presented for the local cross-axial convection scale, ℓ, to compare with our experimentally measured values in Section 5. At the onset of convection $\left(\widetilde{Ra} \approx 1\right)$, inertial advection is weak, and a balance between the viscous and Coriolis terms dominates in moderate Pr fluids.

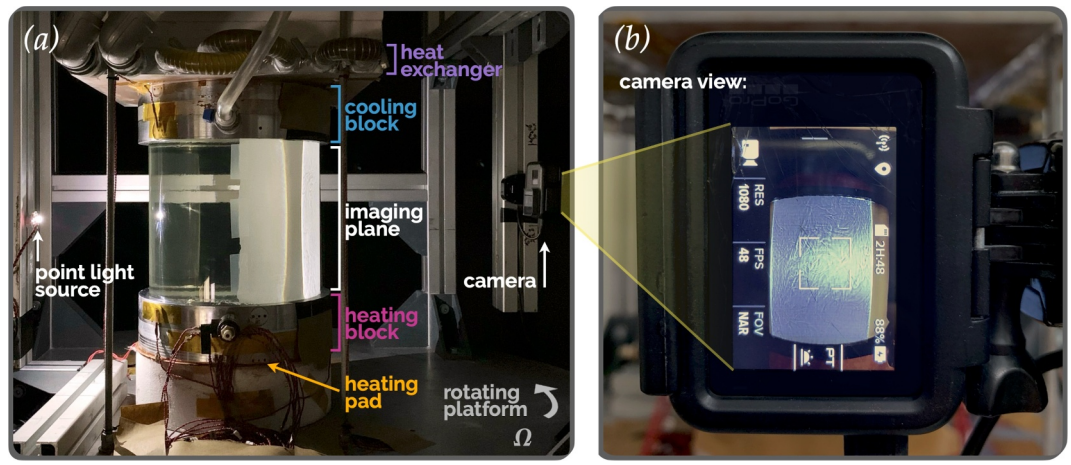

Figure 2. Rotating convection experimental setup with shadowgraph visualization. (a) A diameter $D \approx 20$ cm wide by height $H \approx 20$ cm tall cylindrical convection cell is mounted on a rotating platform and filled with silicone oil. A heating pad warms the bottom of the cell and a recirculating chiller cools the top to drive convection. A point light source positioned at mid-height shines through the silicone oil, casting shadows of the convective plumes' warmer/cooler density contrast onto an imaging plane, which are captured by a camera mounted within the rotating frame of the experiment. (b) Camera point-of-view. The center of the image is over-exposed due to the localized brightness of the point light source and cylindrical distortion.

In this regime, rotating convective flow develops with a cross-axial width estimated to follow the "critical" onset length scale given by

$$\ell_{crit} = 2.4E^{1/3}H \tag{1}$$

for fluids with $Pr > 0.68$ (Chandrasekhar, 1961; Horn & Aurnou, 2022; Julien & Knobloch, 1998). This scale width decreases with decreasing rotation period (decreasing E). Far from the onset of convection $\left(\widetilde{Ra} \gg 1\right)$, fluid motion is expected to be highly turbulent such that the viscous term is negligible, and a vorticity balance between the inertia and Coriolis terms dominates. In this regime, the characteristic width is expected to follow a "turbulent" length scaling given by

$$\ell_{turb} \sim Ro_H^{1/2}H \tag{2}$$

(Aurnou et al., 2020; Featherstone & Hindman, 2016; Guervilly et al., 2019; Hide, 1974; Ingersoll & Pollard, 1982; King & Buffett, 2013; Stevenson, 1979), where Ro_H is the global-scale Rossby number. This dimensionless parameter is defined as $Ro_H = u/(2\Omega H)$, where u is the characteristic flow velocity, and represents the strength of inertial advection on large scales relative to the Coriolis force. Thus, the turbulent scale increases with fluid inertia and decreases with decreasing rotation period.

3. Laboratory Experiment

The experimental setup, pictured in Figure 2a, utilizes a 3D cylindrical convection cell to generate flows representative of those occurring in the polar regions of planetary cores (e.g., Gastine & Aurnou, 2023). The laboratory device used in this study is the same as that described in detail in Abbate and Aurnou (2023) (referred to in-text as AA23 from here onwards). Experiments are conducted using two cylindrical tanks, each with internal diameter $D = 19.29$ cm. One tank measures $H = 19.05$ cm tall (yielding aspect ratio $\Gamma = D/H \simeq 1$) and the other measures $H = 38.10$ cm tall ($\Gamma \simeq 1/2$). The transparent sidewall is made of cast acrylic (thermal conductivity $k = 0.19$ W/m/K) and the top and bottom boundaries are T6061 aluminum ($k = 167$ W/m/K). A non-inductively wound, PID-controlled heat pad warms the bottom boundary to a fixed temperature (T_{bot}), while a recirculating chiller plumbed to an aluminum heat exchanger plate maintains a fixed cool temperature at the top boundary (T_{top}). These temperatures are varied to generate different vertical thermal gradients ($\Delta T = T_{bot} - T_{top}$) and therefore different values of Ra. The convection cell is mounted on a rotary platform programmed to run at a desired angular rotation velocity (Ω), which is varied to investigate multiple E values.

Three different silicone oils, each with a different viscosity (and therefore differing Pr value), are used as the working fluids in the experiments. These oils were chosen specifically for use with our shadowgraph visualization technique detailed in Section 4. The mean temperature of the fluid, measured as $\overline{T} = (T_{bot} + T_{top})/2$, is used to determine temperature-dependent material properties (i.e., density, viscosity, thermal diffusivity). The mean temperature ranges from $25.5 \leq \overline{T} \leq 51.8$°C across experiments, such that Pr varies by up to 25% within each fluid data set. The mean values of Pr, calculated as $Pr \approx 39$, 178, and 836, are therefore used to label the data sets in the figures below. Case-specific parameter values are given in Table B1.

For every experiment, ΔT is measured using six thermistors each embedded within the convection cell's top and bottom thermal blocks. The heating power, $P = IV$, is determined through direct measurements of input voltage, V, and current, I, at the location of the heat pad. The heat flux through the cell is calculated as $q = P/A$, where $A = \pi R^2$ is the active area of the fluid and $R = D/2$ is the internal radius of the convection cell. The non-dimensional heat transfer efficiency, Nusselt number $Nu = qH/(k\Delta T)$, is calculated using the input heating flux (q) and the vertical temperature drop across the cell (ΔT). The cell sidewall is not encased in an insulating thermal blanket in order to enable flow visualization. This allows some of the input heating power to be lost to the surrounding environment, the magnitude of which was not directly measured in this study. Consequently, the determined Nu are artificially increased relative to the actual heat transfer efficiency within the cell (see Figure A1), and are thus not included in the formal analysis. Importantly, however, the experiments were conducted until q and ΔT were constant, allowing for thermal equilibration and accurate Ra number measurements despite sidewall losses.

Flow velocities are estimated for our shadowgraph experiments using the extensive suite of laser Doppler velocimetry measurements made using the same fluids in AA23. Velocities are nondimensionally characterized via the global Reynolds number, $Re_H = uH/\nu$, which defines the strength of inertial advection relative to viscous diffusion. From over 200 rotating convection experiments conducted at varied Ra, E, Pr, and Γ, AA23 report an empirical scaling prediction for the global Reynolds number of

$$Re_H = (0.24 \pm 0.03) Ra^{0.56\pm0.01} E^{0.21\pm0.01} Pr^{-0.94\pm0.01}. \quad (3)$$

Here we use Equation 3 with our control values of Ra, E, and Pr to estimate Re_H for each case. The global Rossby number is calculated via $Ro_H = u/(2\Omega H) = Re_H E$. A notable difference between the experiments of AA23 and those presented here is the lack of thermal insulation in the latter. We thus choose to use the Ra-based best-fit given by Equation 3 to ensure error from thermal losses is not introduced into the Re_H prediction. As such, these velocity estimates are assumed accurate to within the uncertainties reported in Equation 3 for Reynolds numbers $Re_H \gtrsim 10$, which is the lowest value of Re_H measured in AA23. These uncertainties, denoted as δ_{Re_H}, are given in Table B1.

Figure 3 summarizes the parameter space covered in this study. The Ra-E-Pr space is shown in Figure 3a, where color indicates the mean Prandtl number for the fluid data set and dashed lines connect points of approximately constant Ekman number. Boldly colored circular markers show parameters for the $\Gamma \simeq 1$ cell, and faded triangular markers show those for the $\Gamma \simeq 1/2$ cell. Experiments cover dimensional ranges of $8 \lesssim \Delta T \lesssim 74$ K and $0.2 \lesssim \Omega \lesssim 5.1$ rad/s, corresponding to $10^8 \lesssim Ra \lesssim 3 \times 10^{11}$ and $3 \times 10^{-3} \gtrsim E \gtrsim 10^{-6}$. Figure 3b shows Ro_c versus $\widetilde{Ra}$. All experiments are convectively supercritical with $10^2 \lesssim \widetilde{Ra} \lesssim 10^5$. A dotted line at $Ro_c = 1$ marks the predicted regime boundary between weakly rotating and strongly rotating dynamics. Of our 41 experiments, eight cases in the $Pr \approx 178$ and 836 data sets are found to lie in the $Ro_c \gtrsim 1$ weakly rotating regime. Figures 3c and 3d show the estimated Re_H and Ro_H values, respectively. Cases with estimated velocities at $Re_H < 10$ are shown as hollow circles, since Equation 3 only applies to velocities with $Re_H \gtrsim 10$. Figure 3d shows that the global scale Rossby numbers are all well below unity, implying that any large scale motions are strongly affected by rotation. All of the Ra, E, Pr values and the estimated $Re_H \pm \delta_{Re_H}$ values for our experiments are reported in Table B1.

4. Shadowgraph Flow Visualization

We utilize a shadowgraph imaging setup to visualize flow within the cylindrical convection cell. This technique has been implemented in non-rotating laboratory convection experiments utilizing high viscosity oils and syrups (Huang & Xia, 2016; Li et al., 2021; Shang et al., 2003; Xi et al., 2004), but has not been previously employed in a rapidly rotating setup. Shown in Figure 2a, a point light source located approximately 13 cm outside of the cell

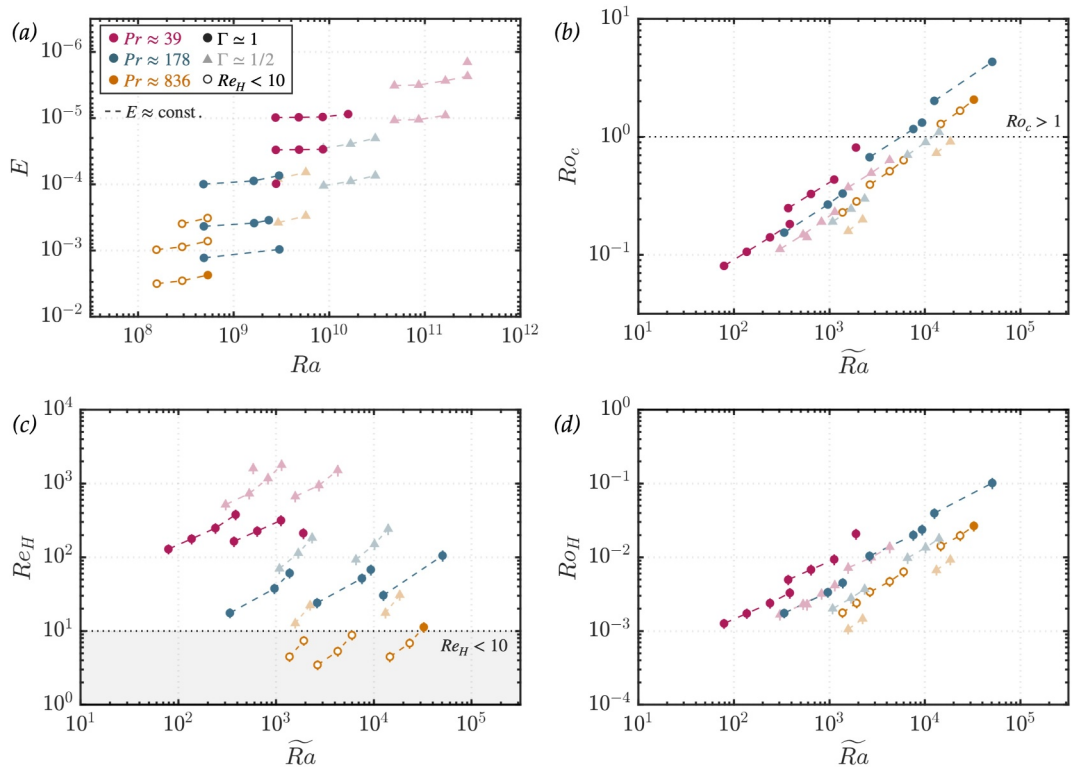

Figure 3. (a) The *Ra*-*E*-*Pr* parameter space of the experiments conducted; (b) Values of Ro_c for the experiments versus the supercriticality $\widetilde{Ra}$; (c) The global Reynolds numbers Re_H and (d) global Rossby numbers Ro_H calculated from Equation 3 using the control parameters of *Ra*, *E*, and *Pr*, each versus the supercriticality. In all panels: marker color indicates Prandtl number, where bold circular points are data with $\Gamma \simeq 1$ and faded triangular points are $\Gamma \simeq 1/2$. Hollow points are at estimated $Re_H < 10$. Dashed lines connect points of approximately constant Ekman number. Vertical error bars in panels (c) and (d) are determined from uncertainties reported in Equation 3. All other error bars are smaller than the marker size.

sidewall shines through the silicone oil, illuminating the 3D space of the tank. The convex curvature of the cylindrical sidewall bends the light emanating from the point source into relatively parallel lines as it passes through the tank, which mitigates distortion effects for the majority of the tank volume. This is demonstrated using the online interactive 2D ray tracing tool from Tu (2016). At https://bit.ly/ray-cyl, we provide an example with our setup parameters. The silicone oil's high coefficient of thermal expansion ($\alpha \approx 10^{-3}$ 1/K) promotes strong temperature-dependent density and index of refraction variations (e.g., Settles & Hargather, 2017). Consequently, the relatively warm or cool convective structures refract the light such that shadows of their shape are cast onto an imaging plane. Here, the imaging plane is a sheet of tracing paper wrapped around the tank's sidewall. The projected shadows are then captured by a camera mounted within the rotating frame, shown in Figure 2b.

Shadowgraph imaging works best when the density-dependent refractive contrasts of the working fluid are high. As such, experiments are largely conducted at high ΔT (and therefore relatively high *Ra*) to maximize the visual contrast. If ΔT is too low ($\approx$10 K or less), the structures appear too faint to analyze. Similarly, water ($Pr \approx 6$) is not considered here due to its relatively low coefficient of thermal expansion $\alpha \approx 10^{-4}$ 1/K. With its α value a full order of magnitude lower than that of silicone oil, water experiments yielded no discernible shadowgraph signals.

Images captured from each experiment are analyzed to extract a measured characteristic cross-axial length scale, ℓ_{meas}. Example images from each *Pr* and Γ data set are shown in Figure 4. From the projected shadows, we see strongly anisotropic rotating convective flow structures, with longer scales in the axial, vertical direction and smaller scales in the cross-axial, horizontal directions. For each case, approximately $N_\ell = 5$–20 of these smaller scale structure widths are hand-measured for a single image, examples of which are highlighted in yellow in Figure 4. Distortion of light is minimal throughout, but increases close to the lateral edges of the illuminated portion of the image, resulting in horizontally squished structures. This region is excluded from the analysis.

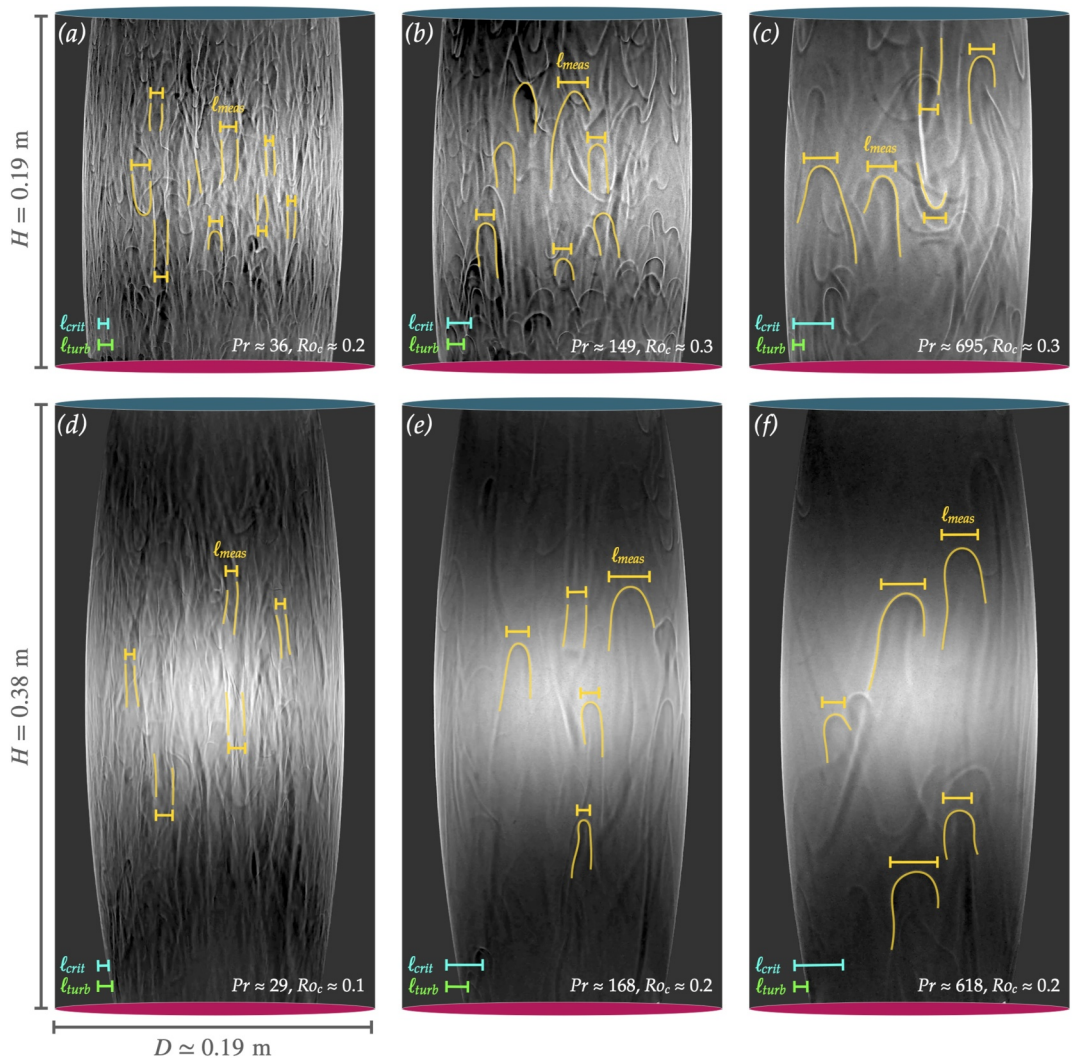

Figure 4. Shadowgraph flow visualization. Panels (a), (b), and (c) show images from the $\Gamma \simeq 1$ cell. Panels (d), (e), and (f) show images from the $\Gamma \simeq 1/2$ cell. Flow structures are visible due to the dark/light contrast of relatively cool/warm regions of the flow as plumes move through the cell. For example, a warm plume originating at the lower boundary moves up through relatively cooler bulk fluid such that a distinct light-shaded curve marks its location as it traverses the tank. Yellow lines demonstrate examples of length scale measurements, ℓ_{meas}. The illuminated portion of the image laterally covers tank radii $s \lesssim 0.8R$. Approximately $N_\ell = 5$–20 structure widths are measured for each case, where the average constitutes the final measurement, $\overline{\ell}_{meas}$, and the standard deviation represents the error, σ_ℓ, for the measurement. The theoretical predictions for the onset and turbulent length scales, given by Equations 1 and 2, are included as teal and green scale bars, respectively. The parameters for the displayed cases are italicized in Table B1.

Further, the outer 20% of the tank diameter is unlit due to the setup geometry. The number of pixels across each structure is converted to a length by assuming the width of the illuminated portion of the image is equal to $d = 0.8D$, where D is the internal diameter of the cell. This assumption does not mathematically account for all lateral distortion, nor spatial variation of the plumes within the tank volume, and is therefore less accurate than comparable particle image velocimetry measurements (e.g., Shi et al., 2020). The measured widths are then averaged for each image to yield the mean length scale estimate, $\overline{\ell}_{meas}$. The error for this measurement is determined as the standard deviation, σ_ℓ, of the counted widths. Values of $\overline{\ell}_{meas} \pm \sigma_\ell$ and the number of structures used in the calculation N_ℓ are reported in Table B1.

We additionally use $\overline{\ell}_{meas}$ to estimate the local convection-scale flow velocities for the experiments. These are the local-scale Reynolds number, given by

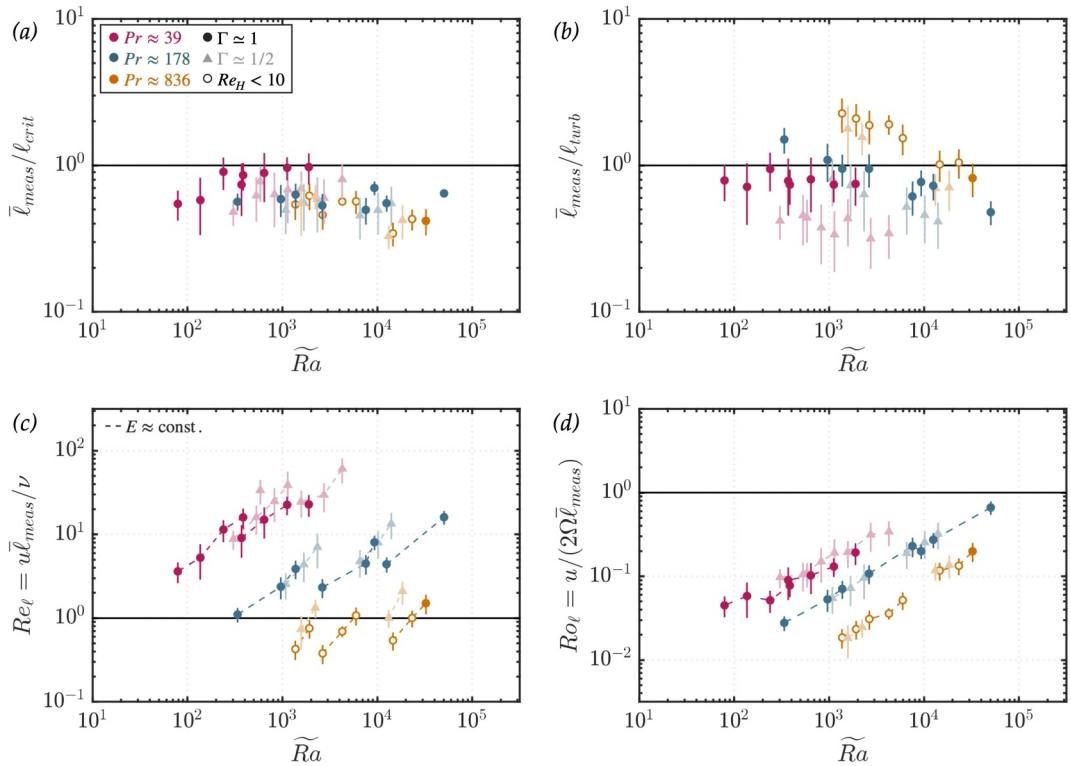

Figure 5. Length scale measurement results. Panels (a) and (b) show the measured scales, $\overline{\ell}_{meas}$, normalized by the theoretical predictions, ℓ_{crit} and ℓ_{turb}, respectively, plotted against the supercriticality, $\widetilde{Ra}$. The solid black line indicates $\overline{\ell}_{meas} = \ell_{theory}$. Vertical error bars in panel (a) account for the standard deviation, σ_ℓ, calculated for each scale measurement, whereas those in panel (b) additionally account for uncertainty reported in Equation 3. Panels (c) and (d) show the local Reynolds number, Re_ℓ, and local Rossby number, Ro_ℓ, respectively. Error bars are calculated as the error in the estimated Re_H calculation given by Equation 3 propagated with σ_ℓ. Marker notation is the same as that in Figure 3.

$$Re_\ell = u\ell/\nu = Re_H(\ell/H), \tag{4}$$

and the local-scale Rossby number, given by

$$Ro_\ell = u/(2\Omega\ell) = Ro_H(H/\ell) = Re_H E(H/\ell). \tag{5}$$

In these calculations, Re_H is given by Equation 3 and $\ell = \overline{\ell}_{meas}$. Errors are computed as a combination of the uncertainty in Re_H and ℓ_{meas}, given by δ_{Re_H} and σ_ℓ, respectively.

5. Scaling Results

The measured length scales $\overline{\ell}_{meas}$, normalized by the theoretical predictions of ℓ_{crit} and ℓ_{turb}, are plotted as a function of the convective supercriticality $\widetilde{Ra}$ in Figures 5a and 5b. Vertical error bars in panel (a) depend solely on the shadowgraph length scale errors, σ_ℓ, whereas error bars in (b) additionally depend on our use of Equation 3 in calculating ℓ_{turb}, and are thus larger. Points with estimated $Re_H < 10$ are denoted with hollow markers in both panels for consistency, however, we note that the result shown in panel (a) does not rely on the Re_H estimate. There is a visible offset between the $\Gamma \simeq 1$ (boldly colored circles) and the $\Gamma \simeq 1/2$ (faded triangles) data sets, particularly noticeable in panel (b) (as well in Figure 7a below). This may indicate an aspect ratio dependence for the local scale, however, the imaging setup was altered slightly between experiments conducted with each tank in order to accommodate the taller convection cell. Consequently, the projection of structures' shadows may not be directly comparable between the two Γ data sets, limiting interpretation of this offset.

Notably, the results in Figures 5a and 5b demonstrate that the measured length scales are simultaneously near both the onset and turbulent cross-axial scaling predictions. Both ratios, $\overline{\ell}_{meas}/\ell_{crit}$ and $\overline{\ell}_{meas}/\ell_{turb}$, remain well within an order of magnitude of unity across all experiments which span $10^2 \lesssim \widetilde{Ra} \lesssim 10^5$. A close correlation with the onset scale may seem unexpected for this parameter range given the large values of supercriticality, yet many cases are scaling with ℓ_{crit} directly, in good agreement with the arguments of Nicoski et al. (2024). The turbulent scale provides an excellent prediction for the $Pr \approx 39$ flows at $\Gamma \simeq 1$, with decreasing agreement as Pr increases. Although the supercriticalities are high for the $Pr \approx 178$ and 836 flows, the Reynolds number estimates indicate that they are still rather laminar (e.g., Figures 3c and 5c where $Re_\ell \approx 1-10$). This implies that the supercriticality needed to yield turbulent rotating convection scales increases significantly with Prandtl number.

Figures 5c and 5d show the estimated values of the local Reynolds number (Re_ℓ) and the local Rossby number (Ro_ℓ), respectively. Most rotating $E \lll 1$ geophysical systems are expected to be characterized by a high local Reynolds number (strong turbulence) and low local Rossby number (strong rotation). In our study, this regime is best achieved with experiments conducted at $Pr \approx 39$. However, these measurements are also the most closely matched to both the onset and turbulent scale predictions, with each yielding excellent agreement with the predictions for much of the $Pr \approx 39$ data set as shown by Figures 5a and 5b. Thus we interestingly find a simultaneous co-scaling with both the onset and turbulent scales even at our most geophysically relevant parameters.

6. Discussion

6.1. Co-Scaling Arguments

The $\overline{\ell}_{meas}$ co-scaling behavior generates ambiguity in how we can interpret the presence of these theoretical scales in physical experiments relevant to geophysical and astrophysical systems (Abbate & Aurnou, 2023; Guervilly et al., 2019; Hawkins et al., 2023; Nicoski et al., 2024; Oliver et al., 2023; Schwaiger et al., 2021). Alternatively put, the correlation of our measured length scales, $\overline{\ell}_{meas}$, with both the critical onset scale, ℓ_{crit}, and the turbulent scale, ℓ_{turb}, poses a rotating convective conundrum. Accurate extrapolations are built upon robust experimental and theoretical congruence. However, one cannot disambiguate the two theoretical scalings in the experimental data. Our coverage is relatively wide across supercriticality $\left(10^2 \lesssim \widetilde{Ra} \lesssim 10^5\right)$, convective Rossby number ($10^{-1} \lesssim Ro_c \lesssim 10^1$), and predicted Reynolds number ($10^1 \lesssim Re_H \lesssim 10^3$), and is generally representative of typical parameters considered in laboratory-numerical rotating convection studies. Here we extend the arguments of AA23 and Hawkins et al. (2023), who demonstrate a link between the two theoretical scales upon finding the same length scale ambiguity in velocity-based studies.

Following Hawkins et al. (2023), we examine the criterion that yields an approximate equivalence between the onset and turbulent length scales, $\ell_{turb} \simeq \ell_{crit}$. First equating their definitions,

$$Ro_H^{1/2} \simeq 2.4E^{1/3}, \tag{6}$$

then substituting $Ro_H = Re_H E$ and simplifying yields

$$Re_H E^{1/3} \simeq 2.4^2. \tag{7}$$

Taking $E^{1/3} = \ell_{crit}/(2.4H)$, Equation 7 becomes

$$Re_H \ell_{crit}/(2.4H) \simeq 2.4^2. \tag{8}$$

Assuming $\ell_{turb} \simeq \ell_{crit} \equiv \ell$ defines $Re_H \ell_{crit}/H \equiv Re_\ell$. Substituting this into Equation 8 gives

$$Re_\ell \simeq 2.4^3 = 14. \tag{9}$$

Thus, we show that $\ell_{turb} \simeq \ell_{crit}$ when $Re_\ell \approx O(10)$ in fluids with $Pr > 0.68$. The local Reynolds numbers for our study exist over the range $0.47 < Re_\ell < 76$ (see Figure 5c). Experiments here are therefore effectively within the regime in which the two scales are likely indistinguishable, consistent with Figures 5a and 5b. The local Reynolds

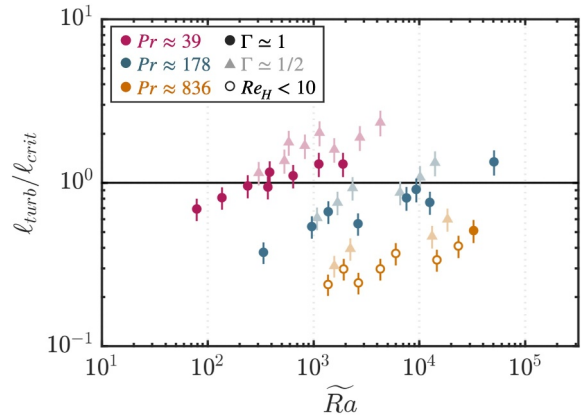

Figure 6. Co-scaling of ℓ_{turb} and ℓ_{crit} across supercriticality, where $\ell_{turb}/\ell_{crit} = Ro_H^{1/2}/(2.4E^{1/3})$. Vertical error bars account for the uncertainty in Equation 3 used to estimate Ro_H.

number must be $Re_\ell \gg 1$, while maintaining $Ro_\ell \ll 1$, in order for scale separation to occur in RRBC (e.g., Nicoski et al., 2024).

Figure 6 provides a direct comparison of the turbulent and onset scales by plotting their ratio, ℓ_{turb}/ℓ_{crit}, against supercriticality, following AA23. Consistent with the local Reynolds number scaling arguments, the ratio remains near unity to within an order of magnitude across the range of Pr and $\widetilde{Ra}$ considered here. In order to analyze behavior at an extended parameter range, AA23 report a best-fit collapse for this ratio of

$$\ell_{\text{turb}}/\ell_{\text{crit}} = (2.0 \pm 0.2)\widetilde{Ra}^{0.21\pm0.01} Pr^{-0.48\pm0.02}. \tag{10}$$

This relation demonstrates a shallow dependence on supercriticality. Extreme values of $\widetilde{Ra}$ are thus needed to achieve a significant separation of the turbulent and onset length scales ($\ell_{turb}/\ell_{crit} \gg 1$), consistent with the need for high local Reynolds numbers. Such high supercriticalities are generally unattainable in rapidly rotating ($E \ll 1$) convection experiments. Even in Earth's outer core at $E \simeq 10^{-15}$ and $Ra \simeq 10^{24}$ (Cheng & Aurnou, 2016), Equation 10 predicts a scale separation of only $\ell_{turb}/\ell_{crit} \simeq 10$ when using the turbulent Prandtl number estimate of $Pr \approx 1$.

Alternatively, we present an equation for the co-scale ratio built from the result of our length scale measurements shown in Figures 5a and 5b. The measurements do not deviate far from the theoretical predictions, so we formulate the ratio with pre-factors of unity for simplicity:

$$\ell_{turb}/\ell_{crit} = Ro_H^{1/2}/(2.4E^{1/3}). \tag{11}$$

This formulation enables direct predictions of the scale separation in planetary systems given an estimated flow velocity.

6.1.1. Local Scales in Earth's Core

In Earth's outer core, flow speeds determined via inversion of geomagnetic secular variation data typically yield $Ro_H \approx 10^{-6}$ (Jackson & Finlay, 2015). Given an outer core thickness of $H \simeq 2{,}255$ km, we calculate the turbulent length scale as $\ell_{turb} = Ro_H^{1/2} H \simeq 2$ km. In contrast, the critical length scale is found to be $\ell_{crit} = 2.4E^{1/3}H \simeq 50$ m, assuming $E \simeq 10^{-15}$ for the core. The scale separation in Earth's core would thus be $\ell_{turb}/\ell_{crit} \simeq 40$, exceeding the estimate provided by Equation 10.

In contrast to both Equations 10 and 11, the low Pr quasi-geostrophic spherical models by Guervilly et al. (2019) suggest an even larger separation, with $\ell_{turb}/\ell_{crit} \simeq 10^3$ in the core. They report a turbulent scale dependence of $\ell/R = 11Ro_H^{1/2}$, where R is the spherical radius defining the global length scale for their model. Assuming the

onset scale in Earth's core follows $\ell_{crit}/R \sim E^{1/3}$, they derive a ratio $11Ro_H^{1/2}/E^{1/3} \simeq 10^3$. Here, we find that the length scales measured in our lowest Pr data set are well described by $\ell/H = Ro_H^{1/2}$ with a pre-factor just under unity (see Figure 5b). Additionally, the plane layer onset prediction $\ell_{crit}/H = 2.4E^{1/3}$ adequately describes this same data set (see Figure 5a). Plane layer theory has been shown to agree well with the polar regions of spherical shells (Gastine & Aurnou, 2023). As such, we formulate our ratio as $Ro_H^{1/2}/\left(2.4E^{1/3}\right) \simeq 40$. To resolve the discrepancy between the findings of Guervilly et al. (2019) and our study, it may be necessary to acquire convective length scale measurements in rotating low Prandtl number liquid metals.

6.1.2. Local Scales in a Subsurface Ocean

The dimensions of liquid water subsurface oceans within the icy satellites of our solar system are not tightly constrained, though the thicknesses are known to be significantly less than that of Earth's outer core. Estimates range from $H \approx$ 10–500 km, depending on the ocean world and the models used in the prediction (Soderlund, 2019). Using Jupiter's moon Europa as an example, its ocean is estimated to be approximately $H \approx 100$ km thick (Anderson et al., 1998), with a viscosity comparable to that of seawater ($\nu \simeq 1.8 \times 10^{-6}$ m^2/s, Nayar et al., 2016), and a global rotation rate of $\Omega = 2 \times 10^{-5}$ s^{-1}. The Ekman number is then estimated as $E = \nu/(2\Omega H) \simeq 10^{-12}$ and the onset length scale is $\ell_{crit} = 2.4E^{1/3}H \simeq 24$ m, not dissimilar from that of Earth's core.

Estimating the turbulent scale is more challenging because flow speeds are even less constrained. One method for predicting flow speed is to use a rotating convection scaling equation, such as that given by Equation 3, to determine the global Reynolds number given known Rayleigh, Ekman, and Prandtl numbers. The Rayleigh number is also unconstrained for subsurface oceans. Though it is estimated for Europa to be in the range of $10^{20} \lesssim Ra \lesssim 10^{22}$ (Soderlund, 2019) based on heat transfer scaling laws from Gastine et al. (2016). Substituting these values for Ra, $E \simeq 10^{-12}$, and $Pr \simeq 11$ into Equation 3 yields a global Reynolds number prediction of $10^7 \lesssim Re_H \lesssim 10^8$ and a global Rossby number prediction of $10^{-4} \gtrsim Ro_H \gtrsim 10^{-5}$. Notably, this extrapolation implies that the global Rossby number in Europa's ocean is far below unity (cf. Soderlund et al., 2014). The turbulent length scale is then calculated to be $\ell_{turb} = Ro^{1/2}H \simeq 10^2$–$10^3$ m, and the ratio of scales is $\ell_{turb}/\ell_{crit} \simeq 5$–50, values also similar to that of Earth's core. Results from the Europa Clipper (Pappalardo et al., 2024) and JUICE (Grasset et al., 2013) missions will likely provide better constraints to improve estimates of the local scales and associated ocean dynamics for the Jovian ocean worlds.

6.2. Comparison to Asymptotic Scaling Predictions

Many studies of geophysical and astrophysical rotating convection systems employ yet another set of turbulent length and velocity scales (Aurnou et al., 2020; Vasil et al., 2021) that are based on fully diffusivity-free, asymptotic theoretical predictions (Julien et al., 1998, 2012; Sprague et al., 2006). Unlike the inviscid scaling arguments that lead to ℓ_{turb}, these asymptotic estimates further assume that rapidly rotating convection is independent of the fluid's thermal diffusivity. Thus, the heat transfer in this regime is controlled solely by the rotating turbulence in the fluid bulk; the boundary layers are then thermally inert (cf. Bouillaut et al., 2021; Julien et al., 2016).

We denote this turbulent, rapidly rotating asymptotic limit as the "diffusion-free" (DF) scaling, as in AA23. In this regime, the global-scale Rossby number scales as

$$Ro_H \sim Ro_c^2 \equiv Ro_{DF}, \tag{12}$$

such that the turbulent length scale prediction then follows

$$\ell \sim Ro_H^{1/2}H \sim Ro_c H \equiv \ell_{DF}. \tag{13}$$

The ratio of turbulent to onset length scales is then

$$\ell_{DF}/\ell_{crit} \sim Ro_c/E^{1/3} \tag{14}$$

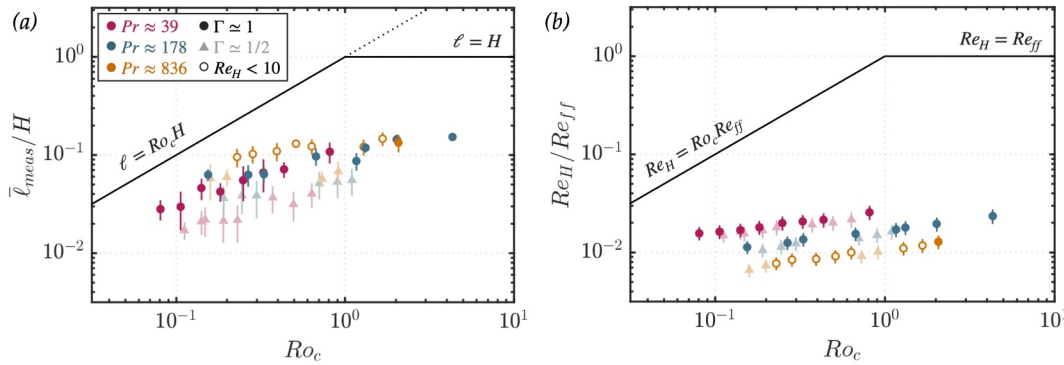

Figure 7. Asymptotic scaling comparison. (a) The measured local length scale, ℓ_{meas}, normalized by the mixing length, H, and (b) the global Reynolds number estimate, Re_H, normalized by the free-fall (or mixing length) Reynolds number, Re_{ff}, each against the convective Rossby number, Ro_c. The diagonal black lines indicate the rotating asymptotic scaling predictions, Equations 12 and 13, plotted here for $Ro_c < 1$. The horizontal black lines indicate the non-rotating asymptotic predictions, Equations 16 and 17, plotted for $Ro_c > 1$. The dotted diagonal line in panel (a) denotes the high Γ, high Ro_c scaling, which cannot develop in our $\Gamma \leq 1$ experiments (but that we include for completeness).

for $Pr > 0.68$ fluids. Re-writing the definition for the convective Rossby number, $Ro_c = \left(RaE^2/Pr\right)^{1/2}$, in terms of the asymptotic supercriticality, $\widetilde{Ra} = RaE^{4/3}$, gives $Ro_c = \left(\widetilde{Ra}/\mathrm{Pr}\right)^{1/2}E^{1/3}$. Substituting this definition into Equation 14 and simplifying yields

$$\ell_{DF}/\ell_{\mathrm{crit}} \sim \left(\widetilde{Ra}/\mathrm{Pr}\right)^{1/2} \tag{15}$$

(cf. Nicoski et al., 2024). Thus, the asymptotic limit of diffusiont-free heat and momentum transfer predicts a supercriticality dependence of $\widetilde{Ra}^{1/2}$ and a Prandtl number dependence of $Pr^{-1/2}$ for the scale separation ratio.

Comparing Equations 10–15, we see a comparable Prandtl number dependence of $Pr^{-0.48}$, but a weaker supercriticality dependence of $\widetilde{Ra}^{0.21}$. This less efficient $\widetilde{Ra}$ scaling is consistent with other RRBC studies (e.g., Hawkins et al., 2023), and is a byproduct of boundary layer throttling of the heat transfer (Aurnou et al., 2020; King et al., 2009; Oliver et al., 2023). In diffusivity-free systems, rotating convective heat transfer is expected to scale as $Nu \sim Ra^{3/2}$ (Bouillaut et al., 2021; Julien et al., 2012). Our measured heat transfer for these experiments instead follows the much less efficient classical, boundary layer controlled heat transfer scaling of $Nu \sim Ra^{1/3}$ (see Figure A1).

In non-rotating convection systems, the asymptotic diffusivity-free scale is often referred to as the "mixing length" (Kraichnan, 1962; Spiegel, 1963, 1971). Without rotational constraint, the non-rotating, diffusivity-free convection freely crosses the vertical length of the system. This turbulent mixing thus defines the convection scale as equivalent to the global convective scale,

$$\ell \simeq H. \tag{16}$$

The associated non-dimensional velocity prediction is commonly called the "free-fall" (*ff*) Reynolds number,

$$Re_H \simeq (Ra/Pr)1/^2 \equiv Re_{ff} \tag{17}$$

Figure 7 shows our (a) shadowgraph length scale measurements and (b) estimated flow velocities plotted relative to the asymptotic scaling predictions given by Equations 12, 13, 16, and 17. Data is shown as colored markers in both Figures 7a and 7b. Solid black lines denote the asymptotic estimates for ℓ and Re_H versus the convective Rossby number, thus marking the upper bounding values of these quantities in rotating convection systems.

For $Ro_c < 1$, the value of ℓ is predicted to follow that of the rapidly rotating limit, $\ell = Ro_c H$, marked as a solid diagonal line in Figure 7a. In low aspect ratio $\Gamma \leq 1$ cells where H is the largest scale in the system, the predicted

Table 2
Estimated Nondimensional Local-Scale Parameters for Earth's Core

ℓ/H	ℓ (m)	Ro_ℓ	Re_ℓ	Rm_ℓ	Λ_ℓ
$Ro_H^{1/2}$	2,500	10^{-3}	10^6	1.4	10
$2.4E^{1/3}$	60	5×10^{-2}	2×10^4	3×10^{-2}	60

Note. Values are calculated using: $u \simeq 4 \times 10^{-4}$ m/s (Jackson & Finlay, 2015), $H \simeq 2{,}255$ km, $\nu \simeq 10^{-6}$ m^2/s, $\eta \simeq 0.7$ m^2/s, $\rho \simeq 1.1 \times 10^4$ kg/m^3, $\Omega \simeq 7.29 \times 10^{-5}$ 1/s (Roberts & King, 2013), and $B \simeq 4$ mT (Gillet et al., 2010).

value changes to that of the non-rotating limit $\ell = H$ when $Ro_c \geq 1$, shown as a solid black horizontal line. In very wide aspect ratio $\Gamma \gg 1$ fluid layers (such as shallow atmospheres), the Coriolis force wraps the flow into large inertial circles with radii of order $Ro_c H$ even when $Ro_c \geq 1$ (e.g., Vieweg et al., 2022). This horizontal scale is referred to as the internal Rossby deformation radius in the oceanic and atmospheric dynamics literature (Cushman-Roisin & Beckers, 2011), and is marked with a dotted diagonal line in Figure 7a. However, the flow scales in our $\Gamma \simeq 1$ and 1/2 experiments cannot exceed $\ell = H$, so this extended $\Gamma \gg 1$, $Ro_c \geq 1$ scaling cannot develop here. The solid black lines in Figure 7b show that similar asymptotic trends exist for Re_H as a function of Ro_c.

The measured length scales and estimated velocities in Figure 7 all plot below the asymptotic predictions. This is unsurprising as the asymptotic predictions approximate the upper bounding values of these quantities. Further, this behavior is expected since the heat transfer in our RRBC experiments is boundary layer limited (see Figure A1), and is thus affected by the fluid's microscale diffusivities in the boundary layers. This limits the energy available to drive convective velocities and to generate larger turbulent flow scales. Interestingly, the positive slope of each Pr data set demonstrates a Ro_c-dependence that implies the presence of rotational effects, even at large $Pr \approx 10^3$ and relatively high $E = 10^{-3}$.

Figure 7 additionally shows that the non-rotating mixing length predictions ($\ell \simeq H$ and $Re_H \simeq Re_{ff}$) cannot adequately describe the properties of rotating $Ro_c \ll 1$ convection systems. The disparity between the rapidly rotating and the non-rotating predictions need not be inconsequential. For instance, in Earth's core we estimate that $Ro_c \sim 10^{-3}$. Such a scaling factor can be of great importance, for instance, when modeling turbulent mixing in stellar and planetary interiors (e.g., Hindman & Fuentes, 2023; Vasil et al., 2021) or dynamo action in planetary cores and magma oceans (e.g., O'Rourke, 2020; Stixrude et al., 2020).

6.3. Planetary Core Magnetohydrodynamic Implications

The local length scales in our experiments are well-predicted by both $\ell_{crit}/H \simeq 2.4E^{1/3}$ and $\ell_{turb}/H \simeq Ro^{1/2}$, with prefactors near unity (see Figures 5a and 5b). This is especially true for the lowest Pr data set considered. As such, we use these local scale predictions to estimate the local-scale magnetohydrodynamic quantities in Earth's core, values which are significant to understanding the driving dynamics behind the geodynamo. These estimates are summarized in Table 2.

On the global scale, the magnetic Reynolds number defines the ratio of magnetic induction to magnetic diffusion across the core and is given by

$$Rm_H = uH/\eta, \tag{18}$$

where η is the magnetic diffusivity. Flow speeds in the core are estimated from secular variation to be $u \simeq 4 \times 10^{-4}$ m/s (Jackson & Finlay, 2015). Using an outer core thickness of $H \simeq 2{,}255$ km and a magnetic diffusivity of $\eta = 0.7$ m^2/s (Roberts & King, 2013), the global magnetic Reynolds number is estimated as $Rm_H \simeq 10^3$, defining Earth's core as a high Rm_H system. The local-scale magnetic Reynolds number is instead defined with the local scale following

$$Rm_\ell = u\ell/\eta = Rm_H(\ell/H). \tag{19}$$

We calculate Equation 19 with both $\ell = \ell_{crit}$ and $\ell = \ell_{turb}$ to find a range of Rm_ℓ supported by our data's simultaneous agreement with both predictions. From the critical scaling, we estimate $\ell = 2.4E^{1/3}H \simeq 60$ m, where $E = \nu/(2\Omega H^2)$ is computed with $\nu \simeq 10^{-6}$ m^2/s and $\Omega \simeq 7.29 \times 10^{-5}$ 1/s (Roberts & King, 2013). From the turbulent scaling, we estimate $\ell = Ro_H^{1/2}H \simeq 2500$ m, where $Ro_H = u/(2\Omega H)$. Substituting these length scale values into Equation 19 estimates a range of $0.03 \lesssim Rm_\ell \lesssim 1.4$, defining Earth's core as a moderately low Rm_ℓ system.

The traditional Elsasser number, which estimates the quasi-static $Rm \lll 1$ Lorentz force relative to the Coriolis force, is given as

$$\Lambda = B^2/\left(2\mu_o \eta \rho \Omega\right), \tag{20}$$

where B is the strength of the magnetic field, μ_o is the magnetic permeability, and ρ is the fluid density (Dormy, 2016; Soderlund et al., 2015). Using $B = 4$ mT (Gillet et al., 2010) and $\rho = 1.1 \times 10^4$ kg/m^3 (Roberts & King, 2013), we calculate $\Lambda \simeq 11$ for Earth's outer core. We further define the local-scale dynamic Elsasser number:

$$\Lambda_\ell \sim \left(\Lambda^2/Rm_\ell\right)^{1/2} \tag{21}$$

(Aurnou & King, 2017; Dormy, 2016; Soderlund et al., 2015). The dynamic Elsasser number estimates the ratio of Lorentz to Coriolis forces acting on the convective scale ℓ and, unlike Λ, is not limited solely to quasi-static low Rm settings. Substituting the predicted range of Rm_ℓ into Equation 21 estimates a dynamic Elsasser range of $60 \gtrsim \Lambda_\ell \gtrsim 10$. These Λ_ℓ values are large, suggesting that local-scale core convective flows operate in the magnetostrophic regime in which Lorentz forces must also be accounted for in addition to rotational effects. Thus, our extrapolations imply that magnetostrophic dynamics must be included in next-generation models of local-scale core turbulence (e.g., Grannan et al., 2022; Guervilly et al., 2019; Horn & Aurnou, 2022; King & Aurnou, 2015; Yadav, Gastine, Christensen, Duarte, & Reiners, 2016).

Table 2 summarizes estimates of a number of the local-scale, non-dimensional parameters in Earth's core. The local Rossby number Ro_ℓ is small consistent with rapid rotation, while the local Elsasser number Λ_ℓ is relatively large, indicating strong magnetic effects. The local Reynolds number Re_ℓ is large, indicating strong small-scale turbulence, while the local magnetic Reynolds number Rm_ℓ is small. This $Re_\ell^{-1} < Ro_\ell < Rm_\ell \lesssim 1$ ordering suggests that deep-seated, convectively driven dynamo generation in Earth's core is likely to occur predominantly via turbulent, mean-field induction processes (e.g., Krause & Rädler, 2016; Moffatt & Dormy, 2019). Planetary dynamo modeling in this regime remains at the edge of what is currently computationally achievable (cf. Schaeffer et al., 2017).

It should further be noted that in the presence of a strong magnetic field, such that the Lorentz force becomes comparable to Coriolis force, the local convective length scale is predicted to increase markedly (Aurnou & King, 2017; Dormy, 2016; Grannan et al., 2022; Horn & Aurnou, 2022; Soderlund et al., 2015; Stellmach & Hansen, 2004; Yadav, Gastine, Christensen, Wolk, & Poppenhaeger, 2016). Such a change in length scale could alter a number of the arguments made herein. Detailed local-scale models of magnetohydrodynamic core turbulence are necessary to investigate this predicted effect, and subsequently compare to hydrodynamic estimates.

7. Conclusions and Open Questions

This work presents the first shadowgraph-based investigation of the scale of local, rotating convective flows in geophysical and astrophysical fluid systems. Using highly refractive silicone oils as the working fluid, our qualitative image analysis demonstrates that the characteristic cross-axial convective scale is comparable to both the critical scale ℓ_{crit} and the turbulent scale ℓ_{turb}. This correlation holds in our data over three orders of magnitude in convective supercriticality. Further, our visualization measurements corroborate the estimated length scales from previous laboratory studies in which the flow velocities (but not the length scales) were directly measured via laser Doppler methods (Abbate & Aurnou, 2023; Hawkins et al., 2023). Our data additionally allows for comparison with the results of direct numerical simulations and laboratory flow imaging techniques such as particle image velocimetry.

This co-scaling behavior represents a troubling conundrum: How do rotating convection scales extrapolate out to planetary cores and stellar convection zones? Are the scales closer to the onset scale (Calkins, 2018; Nicoski et al., 2024) or are they better estimated via turbulent arguments (Aurnou et al., 2020; Featherstone & Hindman, 2016; Guervilly et al., 2019)? Further, if these scales do not separate from one another, what does that mean for the dynamo and convection physics in planetary interiors (cf. Rädler, 1980; Schrinner, 2011)? Following Equation 15, on what scale must future laboratory experiments be built (e.g., Cheng et al., 2018) to achieve a factor of 10^2 to

10^3 separation between the hypothetically distinct turbulent and critical rotating convection length scales? Finally, if these scales refuse to be disambiguated, then their inseparability will require that new theories of rapidly rotating convection physics be developed (e.g., Julien et al., 1998; Oliver et al., 2023).

Appendix A: Measured Heat Transfer

Figure A1 shows global heat transfer measurements acquired during our shadowgraph experiments. The *y*-axis shows *Nu* multiplied by $Pr^{-0.047}$, which is the best-fit *Pr* dependence determined from non-rotating convection data in AA23. The *x*-axis shows the Rayleigh number *Ra*. The solid black line indicates the non-rotating best-fit reported in AA23. The solid gray line indicates the best-fit to the data from this study, which follows:

$$NuPr^{-0.047} = (0.096 \pm 0.013)Ra^{0.319\pm0.006}. \quad \text{(A1)}$$

The pre-factor of 0.096 is 28% higher than the 0.075 prefactor found in AA23. This 28% increase is due to heat that is systematically lost through the shadowgraph setup's uninsulated sidewall (Figure 2a), which is not accounted for in the calculation of *Nu*.

The $Ra^{0.319}$ scaling dependence is in excellent agreement with the results of AA23, indicating that the system is performing as expected despite shadowgraphically necessitated sidewall losses. This $Nu \sim Ra^{1/3}$ heat transfer scaling is also in good agreement with prior convection studies in which boundary layer diffusive properties act to throttle the heat transfer across the fluid bulk (Cheng et al., 2015; Funfschilling et al., 2005). This diffusive throttling acts to limit the convection, leading to lower velocities and smaller turbulent length scales than are predicted for diffusivity-free, turbulent rotating convective flows (e.g., Aurnou et al., 2020; Oliver et al., 2023).

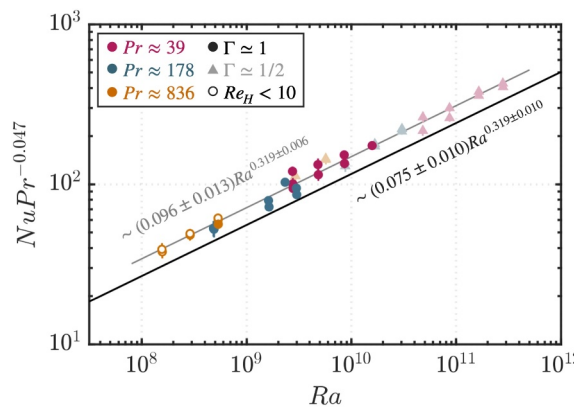

Figure A1. Nondimensional heat transfer efficiency, *Nu*, versus nondimensional buoyancy forcing, *Ra*. The *y*-axis shows *Nu* compensated by the best-fit $Pr^{-0.047}$ dependence found in AA23. The solid black line indicates the best-fit trend from AA23; the solid gray line indicates the best-fit to this study's data. The *Nu* measurements are systematically higher than those in AA23 due to heat losses through the cell's sidewall, which are uninsulated here to allow for the acquisition of shadowgraph imagery.

Appendix B: Data

Table B1 shows the data collected for this study. The first four columns are RRBC experimental control parameters (see Section 2). The fifth column displays Reynolds numbers estimated from the work of Abbate and Aurnou (2023) (see Section 3). The sixth and seventh columns show the convective length scale measurements extracted from shadowgraph images and the standard deviation of the extracted widths, respectively (see Section 4).

Table B1
Rotating Convection Data for $\Gamma \simeq 1$ ($H = 19.05$ cm) and $\Gamma \simeq 1/2$ ($H = 38.10$ cm) Cells

Γ	Pr	E	Ra	$Re_H \pm \delta_{Re_H}$	$(\overline{\ell}_{meas} \pm \sigma_\ell)/H$	N_ℓ
1.01	40.7	9.82E−05	2.78E+09	212 ± 36	(1.08 ± 0.26)E−01	7
1.01	40.7	3.02E−05	2.76E+09	164 ± 26	(5.53 ± 2.15)E−02	11
1.01	40.3	2.99E−05	4.84E+09	227 ± 37	(6.62 ± 2.45)E−02	9
1.01	39.8	2.96E−05	8.60E+09	316 ± 53	(7.15 ± 1.30)E−02	8
1.01	40.7	9.82E−06	2.74E+09	129 ± 20	(2.81 ± 0.66)E−02	9
1.01	40.3	9.73E−06	4.80E+09	178 ± 28	(2.97 ± 1.26)E−02	15
1.01	39.8	9.61E−06	8.54E+09	248 ± 40	(4.62 ± 1.15)E−02	15
1.01	*35.9*	*8.70E−06*	*1.58E+10*	*378 ± 62*	*(4.24 ± 0.91)E−02*	*16*
1.01	201	1.30E−03	4.89E+08	30 ± 5	(1.45 ± 0.18)E−01	5
1.01	150	9.64E−04	3.01E+09	105 ± 18	(1.53 ± 0.10)E−01	4
1.01	201	4.32E−04	4.88E+08	24 ± 4	(9.67 ± 1.94)E−02	8
1.01	180	3.86E−04	1.64E+09	52 ± 8	(8.69 ± 1.78)E−02	7
1.01	163	3.49E−04	2.33E+09	68 ± 11	(1.19 ± 0.13)E−01	5
1.01	201	9.96E−05	4.84E+08	18 ± 3	(6.29 ± 0.83)E−02	9
1.01	179	8.88E−05	1.62E+09	38 ± 6	(6.31 ± 1.56)E−02	18
1.01	*149*	*7.39E−05*	*2.99E+09*	*61 ± 10*	*(6.37 ± 1.19)E−02*	*20*
1.01	955	3.17E−03	1.57E+08	4.5 ± 0.7	(1.21 ± 0.23)E−01	4
1.01	858	2.87E−03	2.90E+08	6.8 ± 1.1	(1.47 ± 0.24)E−01	4
1.01	698	2.36E−03	5.37E+08	11 ± 2	(1.34 ± 0.27)E−01	5
1.01	953	9.74E−04	1.56E+08	3.5 ± 0.5	(1.09 ± 0.23)E−01	6
1.01	857	8.81E−04	2.89E+08	5.3 ± 0.8	(1.31 ± 0.17)E−01	3
1.01	696	7.23E−04	5.36E+08	8.8 ± 1.4	(1.22 ± 0.22)E−01	6
1.01	857	3.95E−04	2.89E+08	4.5 ± 0.7	(9.54 ± 0.21)E−02	6
1.01	*695*	*3.24E−04*	*5.34E+08*	*7.4 ± 1.1*	*(1.02 ± 0.21)E−01*	*5*
0.51	40.1	1.08E−05	4.81E+10	667 ± 115	(3.68 ± 1.14)E−02	6
0.51	39.2	1.05E−05	8.63E+10	943 ± 166	(3.16 ± 1.06)E−02	6
0.51	33.7	9.10E−06	1.64E+11	1,514 ± 272	(4.03 ± 1.12)E−02	6
0.51	40.0	3.23E−06	4.80E+10	517 ± 85	(1.71 ± 0.34)E−02	4
0.51	39.2	3.16E−06	8.64E+10	731 ± 123	(2.19 ± 0.74)E−02	12
0.51	33.7	2.73E−06	1.64E+11	1,173 ± 202	(2.13 ± 0.86)E−02	11
0.51	28.6	2.33E−06	2.80E+11	1,785 ± 313	(2.18 ± 0.90)E−02	11
0.51	*28.6*	*1.43E−06*	*2.79E+11*	*1,604 ± 276*	*(2.10 ± 0.58)E−02*	*10*
0.51	196	1.05E−04	8.74E+09	93 ± 15	(5.15 ± 1.63)E−02	5
0.51	168	9.00E−05	1.68E+10	150 ± 25	(5.33 ± 1.70)E−02	4
0.51	138	7.40E−05	3.04E+10	242 ± 42	(5.55 ± 1.68)E−02	10
0.51	196	2.86E−05	8.68E+09	70 ± 11	(3.64 ± 1.15)E−02	7
0.51	*168*	*2.45E−05*	*1.67E+10*	*114 ± 18*	*(3.86 ± 1.37)E−02*	*6*
0.51	138	2.02E−05	3.03E+10	183 ± 30	(3.86 ± 1.59)E−02	9
0.51	793	3.80E−04	2.92E+09	18 ± 3	(5.71 ± 1.05)E−02	7
0.51	619	3.00E−04	5.69E+09	31 ± 5	(6.80 ± 1.79)E−02	7

Table B1
Continued

Γ	Pr	E	Ra	$Re_H \pm \delta_{Re_H}$	$(\overline{\ell}_{meas} \pm \sigma_\ell)/H$	N_ℓ
0.51	791	8.29E−05	2.91E+09	13 ± 2	(5.79 ± 2.33)E−02	6
0.51	*618*	*6.57E−05*	*5.69E+09*	*22 ± 4*	*(5.96 ± 1.15)E−02*	*9*

Note. Control parameters are Γ, Pr, E, and Ra. Non-dimensional global velocities, $Re_H \pm \delta_{Re_H}$, are calculated using Equation 3. Values of $Re_H < 10$ are shown in gray to note the estimates for which Equation 3 is likely not applicable. Length scales, $\overline{\ell}_{meas}$, are measured from the shadowgraph images (see Figure 4). N_ℓ is the number of structures used to calculate $\overline{\ell}_{meas}$, and σ_ℓ is the standard deviation of the measured widths for each case. Italicized rows correspond to the cases displayed in Figure 4.

Data Availability Statement

The laboratory data, analysis scripts, outputted figures, case images, and Table B1 are available online through Zenodo (Abbate & Aurnou, 2024, https://doi.org/10.5281/zenodo.12193776). An image of the ray tracing simulation with our case parameters is included in the repository. The software used to generate it is also publicly available (Tu, 2016, https://doi.org/10.5281/zenodo.6386611).

Acknowledgments
We thank Mike Calkins and our late colleague Keith Julien for many fruitful discussions, as well as Taylor Lonner and Norris Khoo for their help in setting up early versions of the shadowgraph system. J.A.A. thanks the DoD's NDSEG Fellowship program for graduate support. J.M.A. sincerely thanks the NSF Geophysics Program for support via award #2143939.

References

Abbate, J. A., & Aurnou, J. M. (2023). Rotating convective turbulence in moderate to high Prandtl number fluids. *Geophysical & Astrophysical Fluid Dynamics*, *117*(6), 1–40. https://doi.org/10.1080/03091929.2023.2280874

Abbate, J. A., & Aurnou, J. M. (2024). Shadowgraph measurements of rotating convective planetary core-style flows (data, code, and figures) [Dataset]. *Zenodo*. https://doi.org/10.5281/zenodo.12193776

Anderson, J., Schubert, G., Jacobson, R., Lau, E., Moore, W., & Sjogren, W. (1998). Europa's differentiated internal structure: Inferences from four Galileo encounters. *Science*, *281*(5385), 2019–2022. https://doi.org/10.1126/science.281.5385.2019

Aubert, J., Brito, D., Nataf, H., Cardin, P., & Masson, J. (2001). A systematic experimental study of rapidly rotating spherical convection in water and liquid gallium. *Physics of the Earth and Planetary Interiors*, *128*(1–4), 51–74. https://doi.org/10.1016/s0031-9201(01)00277-1

Aubert, J., Gastine, T., & Fournier, A. (2017). Spherical convective dynamos in the rapidly rotating asymptotic regime. *Journal of Fluid Mechanics*, *813*, 558–593. https://doi.org/10.1017/jfm.2016.789

Aurnou, J. M., Calkins, M., Cheng, J., Julien, K., King, E., Nieves, D., et al. (2015). Rotating convective turbulence in earth and planetary cores. *Physics of the Earth and Planetary Interiors*, *246*, 52–71. https://doi.org/10.1016/j.pepi.2015.07.001

Aurnou, J. M., Horn, S., & Julien, K. (2020). Connections between nonrotating, slowly rotating, and rapidly rotating turbulent convection transport scalings. *Physical Review Research*, *2*(4), 043115. https://doi.org/10.1103/physrevresearch.2.043115

Aurnou, J. M., & King, E. (2017). The cross-over to magnetostrophic convection in planetary dynamo systems. *Proceedings of the Royal Society of London*, *473*(2199), 20160731. https://doi.org/10.1098/rspa.2016.0731

Böning, V. G., Wulff, P., Dietrich, W., Wicht, J., & Christensen, U. R. (2023). Direct driving of simulated planetary jets by upscale energy transfer. *Astronomy & Astrophysics*, *670*, A15. https://doi.org/10.1051/0004-6361/202244278

Bouffard, M., Choblet, G., Labrosse, S., & Wicht, J. (2019). Chemical convection and stratification in the earth's outer core. *Frontiers of Earth Science*, *7*, 99. https://doi.org/10.3389/feart.2019.00099

Bouillaut, V., Miquel, B., Julien, K., Aumaître, S., & Gallet, B. (2021). Experimental observation of the geostrophic turbulence regime of rapidly rotating convection. *Proceedings of the National Academy of Sciences*, *118*(44), e2105015118. https://doi.org/10.1073/pnas.2105015118

Calkins, M. A. (2018). Quasi-geostrophic dynamo theory. *Physics of the Earth and Planetary Interiors*, *276*, 182–189. https://doi.org/10.1016/j.pepi.2017.05.001

Calkins, M. A., Julien, K., Tobias, S. M., & Aurnou, J. M. (2015). A multiscale dynamo model driven by quasi-geostrophic convection. *Journal of Fluid Mechanics*, *780*, 143–166. https://doi.org/10.1017/jfm.2015.464

Calkins, M. A., Noir, J., Eldredge, J. D., & Aurnou, J. M. (2012). The effects of boundary topography on convection in Earth's core. *Geophysical Journal International*, *189*(2), 799–814. https://doi.org/10.1111/j.1365-246x.2012.05415.x

Calkins, M. A., Orvedahl, R. J., & Featherstone, N. A. (2021). Large-scale balances and asymptotic scaling behaviour in spherical dynamos. *Geophysical Journal International*, *227*(2), 1228–1245. https://doi.org/10.1093/gji/ggab274

Camisassa, M. E., & Featherstone, N. A. (2022). Solar-like to antisolar differential rotation: A geometric interpretation. *The Astrophysical Journal*, *938*(1), 65. https://doi.org/10.3847/1538-4357/ac879f

Cardin, P., & Olson, P. (1994). Chaotic thermal convection in a rapidly rotating spherical shell: Consequences for flow in the outer core. *Physics of the Earth and Planetary Interiors*, *82*(3–4), 235–259. https://doi.org/10.1016/0031-9201(94)90075-2

Chandrasekhar, S. (1961). *Hydrodynamic and hydromagnetic stability*. Oxford.

Cheng, J. S., & Aurnou, J. M. (2016). Tests of diffusion-free scaling behaviors in numerical dynamo datasets. *Earth and Planetary Science Letters*, *436*, 121–129. https://doi.org/10.1016/j.epsl.2015.12.004

Cheng, J. S., Aurnou, J. M., Julien, K., & Kunnen, R. P. (2018). A heuristic framework for next-generation models of geostrophic convective turbulence. *Geophysical & Astrophysical Fluid Dynamics*, *112*(4), 277–300. https://doi.org/10.1080/03091929.2018.1506024

Cheng, J. S., Madonia, M., Guzmán, A. J. A., & Kunnen, R. P. (2020). Laboratory exploration of heat transfer regimes in rapidly rotating turbulent convection. *Physical Review Fluids*, *5*(11), 113501. https://doi.org/10.1103/physrevfluids.5.113501

Cheng, J. S., Stellmach, S., Ribeiro, A., Grannan, A., King, E. M., & Aurnou, J. M. (2015). Laboratory-numerical models of rapidly rotating convection in planetary cores. *Geophysical Journal International*, *201*(1), 1–17. https://doi.org/10.1093/gji/ggu480

Christensen, U. R. (2010). Dynamo scaling laws and applications to the planets. *Space Science Reviews*, *152*(1–4), 565–590. https://doi.org/10.1007/s11214-009-9553-2
Cushman-Roisin, B., & Beckers, J.-M. (2011). *Introduction to geophysical fluid dynamics: Physical and numerical aspects*. Academic press.
Davidson, P. (2013). Scaling laws for planetary dynamos. *Geophysical Journal International*, *195*(1), 67–74. https://doi.org/10.1093/gji/ggt167
Dormy, E. (2016). Strong-field spherical dynamos. *Journal of Fluid Mechanics*, *789*, 500–513. https://doi.org/10.1017/jfm.2015.747
Dziewonski, A. M., & Anderson, D. L. (1981). Preliminary reference Earth model. *Physics of the Earth and Planetary Interiors*, *25*(4), 297–356. https://doi.org/10.1016/0031-9201(81)90046-7
Featherstone, N. A., & Hindman, B. W. (2016). The emergence of solar supergranulation as a natural consequence of rotationally constrained interior convection. *ApJL*, *830*(1), L15. https://doi.org/10.3847/2041-8205/830/1/l15
Funfschilling, D., Brown, E., Nikolaenko, A., & Ahlers, G. (2005). Heat transport by turbulent Rayleigh–Bénard convection in cylindrical samples with aspect ratio one and larger. *Journal of Fluid Mechanics*, *536*, 145–154. https://doi.org/10.1017/s0022112005005057
Gastine, T., & Aurnou, J. M. (2023). Latitudinal regionalization of rotating spherical shell convection. *Journal of Fluid Mechanics*, *954*, R1. https://doi.org/10.1017/jfm.2022.1010
Gastine, T., Wicht, J., & Aubert, J. (2016). Scaling regimes in spherical shell rotating convection. *Journal of Fluid Mechanics*, *808*, 690–732. https://doi.org/10.1017/jfm.2016.659
Gastine, T., Yadav, R. K., Morin, J., Reiners, A., & Wicht, J. (2013). From solar-like to antisolar differential rotation in cool stars. *Monthly Notices of the Royal Astronomical Society*, *438*(1), L76–L80. https://doi.org/10.1093/mnrasl/slt162
Gillet, N., Brito, D., Jault, D., & Nataf, H. (2007). Experimental and numerical studies of convection in a rapidly rotating spherical shell. *Journal of Fluid Mechanics*, *580*, 83–121. https://doi.org/10.1017/s0022112007005265
Gillet, N., Jault, D., Canet, E., & Fournier, A. (2010). Fast torsional waves and strong magnetic field within the earth's core. *Nature*, *465*(7294), 74–77. https://doi.org/10.1038/nature09010
Grannan, A. M., Cheng, J. S., Aggarwal, A., Hawkins, E. K., Xu, Y., Horn, S., et al. (2022). Experimental pub crawl from Rayleigh–Bénard to magnetostrophic convection. *Journal of Fluid Mechanics*, *939*, R1. https://doi.org/10.1017/jfm.2022.204
Grasset, O., Dougherty, M., Coustenis, A., Bunce, E., Erd, C., Titov, D., et al. (2013). Jupiter icy moons explorer (juice): An ESA mission to orbit Ganymede and to characterise the Jupiter system. *Planetary and Space Science*, *78*, 1–21. https://doi.org/10.1016/j.pss.2012.12.002
Guervilly, C., Cardin, P., & Schaeffer, N. (2019). Turbulent convective length scale in planetary cores. *Nature*, *570*(7761), 368–371. https://doi.org/10.1038/s41586-019-1301-5
Hawkins, E. K., Cheng, J. S., Abbate, J. A., Pilegard, T., Stellmach, S., Julien, K., & Aurnou, J. M. (2023). Laboratory models of planetary core-style convective turbulence. *Fluids*, *8*(4), 106. https://doi.org/10.3390/fluids8040106
Hide, R. (1974). Jupiter and Saturn. *Proceedings of the Royal Society of London*, *336*(1604), 63–84.
Hindman, B. W., & Fuentes, J. (2023). Dwindling surface cooling of a rotating Jovian planet leads to a convection zone that grows to a finite depth. *ApJL*, *957*(2), L23. https://doi.org/10.3847/2041-8213/ad0642
Horn, S., & Aurnou, J. M. (2022). The Elbert range of magnetostrophic convection. I. linear theory. *Proceedings of the Royal Society of London*, *478*(2264), 20220313. https://doi.org/10.1098/rspa.2022.0313
Huang, S.-D., & Xia, K.-Q. (2016). Effects of geometric confinement in quasi-2-D turbulent Rayleigh–Bénard convection. *Journal of Fluid Mechanics*, *794*, 639–654. https://doi.org/10.1017/jfm.2016.181
Ingersoll, A. P., & Pollard, D. (1982). Motion in the interiors and atmospheres of Jupiter and Saturn: Scale analysis, Anelastic equations, Barotropic stability criterion. *Icarus*, *52*(1), 62–80. https://doi.org/10.1016/0019-1035(82)90169-5
Jackson, A., & Finlay, C. (2015). Geomagnetic secular variation and its applications to the core. *Treatise on Geophysics*, 137–184. https://doi.org/10.1016/b978-0-444-53802-4.00099-3
Julien, K., Aurnou, J. M., Calkins, M. A., Knobloch, E., Marti, P., Stellmach, S., & Vasil, G. M. (2016). A nonlinear model for rotationally constrained convection with Ekman pumping. *Journal of Fluid Mechanics*, *798*, 50–87. https://doi.org/10.1017/jfm.2016.225
Julien, K., & Knobloch, E. (1998). Strongly nonlinear convection cells in a rapidly rotating fluid layer: The tilted f-plane. *Journal of Fluid Mechanics*, *360*, 141–178. https://doi.org/10.1017/s0022112097008446
Julien, K., Knobloch, E., Rubio, A. M., & Vasil, G. M. (2012). Heat transport in low-Rossby-number Rayleigh-Bénard convection. *Physical Review Letters*, *109*(25), 254503. https://doi.org/10.1103/physrevlett.109.254503
Julien, K., Knobloch, E., & Werne, J. (1998). A new class of equations for rotationally constrained flows. *Theoretical and Computational Fluid Dynamics*, *11*(3–4), 251–261. https://doi.org/10.1007/s001620050092
Kennett, B. L. N. (2020). Radial Earth models revisited. *Geophysical Journal International*, *222*(3), 2189–2204. https://doi.org/10.1093/gji/ggaa298
King, E. M., & Aurnou, J. M. (2015). Magnetostrophic balance as the optimal state for turbulent magnetoconvection. *Proceedings of the National Academy of Sciences*, *112*(4), 990–994. https://doi.org/10.1073/pnas.1417741112
King, E. M., & Buffett, B. A. (2013). Flow speeds and length scales in geodynamo models: The role of viscosity. *Earth and Planetary Science Letters*, *371*, 156–162. https://doi.org/10.1016/j.epsl.2013.04.001
King, E. M., Stellmach, S., & Aurnou, J. M. (2012). Heat transfer by rapidly rotating Rayleigh–Bénard convection. *Journal of Fluid Mechanics*, *691*, 568–582. https://doi.org/10.1017/jfm.2011.493
King, E. M., Stellmach, S., Noir, J., Hansen, U., & Aurnou, J. M. (2009). Boundary layer control of rotating convection systems. *Nature*, *457*(7227), 301–304. https://doi.org/10.1038/nature07647
Kraichnan, R. H. (1962). Turbulent thermal convection at arbitrary Prandtl number. *Physics of Fluids*, *5*(11), 1374–1389. https://doi.org/10.1063/1.1706533
Krause, F., & Rädler, K.-H. (2016). *Mean-field magnetohydrodynamics and dynamo theory*. Elsevier.
Kunnen, R. P. J. (2021). The geostrophic regime of rapidly rotating turbulent convection. *Journal of Turbulence*, *22*(4–5), 267–296. https://doi.org/10.1080/14685248.2021.1876877
Kunnen, R. P. J., Geurts, B. J., & Clercx, H. (2010). Experimental and numerical investigation of turbulent convection in a rotating cylinder. *Journal of Fluid Mechanics*, *642*, 445–476. https://doi.org/10.1017/s002211200999190x
Li, X.-M., He, J.-D., Tian, Y., Hao, P., & Huang, S.-D. (2021). Effects of Prandtl number in quasi-two-dimensional Rayleigh–Bénard convection. *Journal of Fluid Mechanics*, *915*, A60. https://doi.org/10.1017/jfm.2021.21
Liu, Y., & Ecke, R. E. (1997). Heat transport scaling in turbulent Rayleigh-Bénard convection: Effects of rotation and Prandtl number. *Physical Review Letters*, *79*(12), 2257–2260. https://doi.org/10.1103/physrevlett.79.2257
Lonner, T. L., Aggarwal, A., & Aurnou, J. M. (2022). Planetary core-style rotating convective flows in paraboloidal laboratory experiments. *Journal of Geophysical Research: Planets*, *127*(10), e2022JE007356. https://doi.org/10.1029/2022je007356

Lu, H. Y., Ding, G. Y., Shi, J. Q., Xia, K. Q., & Zhong, J. Q. (2021). Heat-transport scaling and transition in geostrophic rotating convection with varying aspect ratio. *Physical Review Fluids*, *6*(7), L071501. https://doi.org/10.1103/physrevfluids.6.l071501
Madonia, M., Guzmán, A. J. A., Clercx, H. J., & Kunnen, R. P. (2021). Velocimetry in rapidly rotating convection: Spatial correlations, flow structures and length scales (a). *Europhysics Letters*, *135*(5), 54002.
Madonia, M., Guzmán, A. J. A., Clercx, H. J., & Kunnen, R. P. (2023). Reynolds number scaling and energy spectra in geostrophic convection. *Journal of Fluid Mechanics*, *962*, A36. https://doi.org/10.1017/jfm.2023.326
Moffatt, K., & Dormy, E. (2019). *Self-exciting fluid dynamos* (Vol. 59). Cambridge University Press. https://doi.org/10.1017/9781107588691
Nakagawa, Y., & Frenzen, P. (1955). A theoretical and experimental study of cellular convection in rotating fluids. *Tellus*, *7*(1), 2–21. https://doi.org/10.3402/tellusa.v7i1.8773
Nayar, K. G., Sharqawy, M. H., Banchik, L. D., & Lienhard V, J. H. (2016). Thermophysical properties of seawater: A review and new correlations that include pressure dependence. *Desalination*, *390*, 1–24. https://doi.org/10.1016/j.desal.2016.02.024
Nicoski, J. A., O'Connor, A. R., & Calkins, M. A. (2024). Asymptotic scaling relations for rotating spherical convection with strong zonal flows. *Journal of Fluid Mechanics*, *981*, A22. https://doi.org/10.1017/jfm.2024.78
Niiler, P. P., & Bisshopp, F. E. (1965). On the influence of Coriolis force on onset of thermal convection. *Journal of Fluid Mechanics*, *22*(4), 753–761. https://doi.org/10.1017/s002211206500112x
Nimmo, F., & Pappalardo, R. T. (2016). Ocean worlds in the outer solar system. *Journal of Geophysical Research: Planets*, *121*(8), 1378–1399. https://doi.org/10.1002/2016je005081
Oliver, T. G., Jacobi, A. S., Julien, K., & Calkins, M. A. (2023). Small scale quasigeostrophic convective turbulence at large Rayleigh number. *Physical Review Fluids*, *8*(9), 093502. https://doi.org/10.1103/physrevfluids.8.093502
O'Rourke, J. G. (2020). Venus: A thick basal magma ocean may exist today. *Geophysical Research Letters*, *47*(4), e2019GL086126. https://doi.org/10.1029/2019gl086126
Pappalardo, R. T., Buratti, B. J., Korth, H., Senske, D. A., Blaney, D. L., Blankenship, D. D., et al. (2024). Science overview of the Europa clipper mission. *Space Science Reviews*, *220*(4), 1–58. https://doi.org/10.1007/s11214-024-01070-5
Rädler, K.-H. (1980). Mean-field approach to spherical dynamo models. *Astronomische Nachrichten*, *301*(3), 101–129. https://doi.org/10.1002/asna.2103010302
Roberts, P. H., & King, E. M. (2013). On the genesis of the earth's magnetism. *Reports on Progress in Physics*, *76*(9), 096801. https://doi.org/10.1088/0034-4885/76/9/096801
Rossby, H. (1969). A study of bénard convection with and without rotation. *Journal of Fluid Mechanics*, *36*(2), 309–335. https://doi.org/10.1017/s0022112069001674
Sakai, S. (1997). The horizontal scale of rotating convection in the geostrophic regime. *Journal of Fluid Mechanics*, *333*, 85–95. https://doi.org/10.1017/s0022112096004168
Schaeffer, N., Jault, D., Nataf, H.-C., & Fournier, A. (2017). Turbulent geodynamo simulations: A leap towards Earth's core. *Geophysical Journal International*, *211*(1), 1–29. https://doi.org/10.1093/gji/ggx265
Schrinner, M. (2011). Global dynamo models from direct numerical simulations and their mean-field counterparts. *Astronomy & Astrophysics*, *533*, A108. https://doi.org/10.1051/0004-6361/201116642
Schwaiger, T., Gastine, T., & Aubert, J. (2019). Force balance in numerical geodynamo simulations: A systematic study. *Geophysical Journal International*, *219*(Supplement_1), S101–S114. https://doi.org/10.1093/gji/ggz192
Schwaiger, T., Gastine, T., & Aubert, J. (2021). Relating force balances and flow length scales in geodynamo simulations. *Geophysical Journal International*, *224*(3), 1890–1904. https://doi.org/10.1093/gji/ggaa545
Settles, G. S., & Hargather, M. J. (2017). A review of recent developments in schlieren and shadowgraph techniques. *Measurement Science and Technology*, *28*(4), 042001. https://doi.org/10.1088/1361-6501/aa5748
Shang, X.-D., Qiu, X.-L., Tong, P., & Xia, K.-Q. (2003). Measured local heat transport in turbulent Rayleigh-Bénard convection. *Physical Review Letters*, *90*(7), 074501. https://doi.org/10.1103/physrevlett.90.074501
Shi, J.-Q., Lu, H.-Y., Ding, S.-S., & Zhong, J.-Q. (2020). Fine vortex structure and flow transition to the geostrophic regime in rotating Rayleigh-Bénard convection. *Physical Review Fluids*, *5*(1), 011501. https://doi.org/10.1103/physrevfluids.5.011501
Soderlund, K. M. (2019). Ocean dynamics of outer solar system satellites. *Geophysical Research Letters*, *46*(15), 8700–8710. https://doi.org/10.1029/2018gl081880
Soderlund, K. M., Schmidt, B., Wicht, J., & Blankenship, D. (2014). Ocean-driven heating of Europa's icy shell at low latitudes. *Nature Geoscience*, *7*(1), 16–19. https://doi.org/10.1038/ngeo2021
Soderlund, K. M., Sheyko, A., King, E. M., & Aurnou, J. M. (2015). The competition between Lorentz and Coriolis forces in planetary dynamos. *Progress in Earth and Planetary Science*, *2*, 1–10. https://doi.org/10.1186/s40645-015-0054-5
Spiegel, E. A. (1963). A generalization of the mixing-length theory of turbulent convection. *The Astrophysical Journal*, *138*, 216. https://doi.org/10.1086/147628
Spiegel, E. A. (1971). Convection in stars I. Basic boussinesq convection. *Annual Review of Astronomy and Astrophysics*, *9*(1), 323–352. https://doi.org/10.1146/annurev.aa.09.090171.001543
Sprague, M., Julien, K., Knobloch, E., & Werne, J. (2006). Numerical simulation of an asymptotically reduced system for rotationally constrained convection. *Journal of Fluid Mechanics*, *551*(-1), 141–174. https://doi.org/10.1017/s0022112005008499
Stellmach, S., & Hansen, U. (2004). Cartesian convection driven dynamos at low Ekman number. *Physical Review E - Statistical Physics, Plasmas, Fluids, and Related Interdisciplinary Topics*, *70*(5), 056312. https://doi.org/10.1103/physreve.70.056312
Stellmach, S., Lischper, M., Julien, K., Vasil, G., Cheng, J. S., Ribeiro, A., et al. (2014). Approaching the asymptotic regime of rapidly rotating convection: Boundary layers versus interior dynamics. *Physical Review Letters*, *113*(25), 254501. https://doi.org/10.1103/physrevlett.113.254501
Stevenson, D. J. (1979). Turbulent thermal convection in the presence of rotation and a magnetic field: A heuristic theory. *Geophysical & Astrophysical Fluid Dynamics*, *12*(1), 139–169. https://doi.org/10.1080/03091927908242681
Stixrude, L., Scipioni, R., & Desjarlais, M. P. (2020). A silicate dynamo in the early Earth. *Nature Communications*, *11*(1), 935. https://doi.org/10.1038/s41467-020-14773-4
Tobias, S. (2021). The turbulent dynamo. *Journal of Fluid Mechanics*, *912*, P1. https://doi.org/10.1017/jfm.2020.1055
Tu, Y.-T. (2016). Ray optics simulation. *Zenodo*. https://doi.org/10.5281/zenodo.6386611
Vasil, G. M., Julien, K., & Featherstone, N. A. (2021). Rotation suppresses giant-scale solar convection. *Proceedings of the National Academy of Sciences*, *118*(31), e2022518118. https://doi.org/10.1073/pnas.2022518118
Vieweg, P. P., Scheel, J. D., Stepanov, R., & Schumacher, J. (2022). Inverse cascades of kinetic energy and thermal variance in three-dimensional horizontally extended turbulent convection. *Physical Review Research*, *4*(4), 043098. https://doi.org/10.1103/physrevresearch.4.043098

Vogt, T., Horn, S., & Aurnou, J. M. (2021). Oscillatory thermal–inertial flows in liquid metal rotating convection. *Journal of Fluid Mechanics*, *911*, A5. https://doi.org/10.1017/jfm.2020.976

Wedi, M., Van Gils, D. P., Bodenschatz, E., & Weiss, S. (2021). Rotating turbulent thermal convection at very large Rayleigh numbers. *Journal of Fluid Mechanics*, *912*, A30. https://doi.org/10.1017/jfm.2020.1149

Weiss, S., & Ahlers, G. (2011). The large-scale flow structure in turbulent rotating Rayleigh–Bénard convection. *Journal of Fluid Mechanics*, *688*, 461–492. https://doi.org/10.1017/jfm.2011.392

Xi, H.-D., Lam, S., & Xia, K.-Q. (2004). From laminar plumes to organized flows: The onset of large-scale circulation in turbulent thermal convection. *Journal of Fluid Mechanics*, *503*, 47–56. https://doi.org/10.1017/s0022112004008079

Yadav, R. K., Gastine, T., Christensen, U. R., Duarte, L., & Reiners, A. (2016). Effect of shear and magnetic field on the heat-transfer efficiency of convection in rotating spherical shells. *Geophysical Journal International*, *204*(2), 1120–1133. https://doi.org/10.1093/gji/ggv506

Yadav, R. K., Gastine, T., Christensen, U. R., Wolk, S. J., & Poppenhaeger, K. (2016). Approaching a realistic force balance in geodynamo simulations. *Proceedings of the National Academy of Sciences*, *113*(43), 12065–12070. https://doi.org/10.1073/pnas.1608998113

Yan, M., & Calkins, M. A. (2022). Strong large scale magnetic fields in rotating convection-driven dynamos: The important role of magnetic diffusion. *Physical Review Research*, *4*(1), L012026. https://doi.org/10.1103/physrevresearch.4.l012026